Extreme multi-valence states in mixed actinide oxides

Epifano, E.; Naji, M.; Manara, D.; Scheinost, A. C.; Hennig, C.; Lechelle, J.; Konings, R. J.M.; Rothe, J.; Martin, P. M.; More Authors

Important note
To cite this publication, please use the final published version (if applicable).
Please check the document version above.

ARTICLE

Extreme multi-valence states in mixed actinide oxides

E. Epifano[1,2,3], M. Naji[4,5], D. Manara[4], A.C. Scheinost[6], C. Hennig[6], J. Lechelle [7], R.J.M. Konings [4], C. Guéneau[8], D. Prieur[6], T. Vitova[9], K. Dardenne[9], J. Rothe[9] & P.M. Martin [1]

To assure the safety of oxide-fuel based nuclear reactors, the knowledge of the atomic-scale properties of $U_{1-y}M_yO_{2\pm x}$ materials is essential. These compounds show complex chemical properties, originating from the fact that actinides and rare earths may occur with different oxidation states. In these mostly ionic materials, aliovalent cationic configurations can induce changes in the oxygen stoichiometry, with dramatic effects on the properties of the fuel. First studies on $U_{1-y}Am_yO_{2\pm x}$ indicated that these materials exhibit particularly complex electronic and local-structure configurations. Here we present an in-depth study of these compounds, over a wide compositional domain, by combining XRD, XAS and Raman spectroscopy. We provide evidences of the co-existence of four different cations (U^{4+}, U^{5+}, Am^{3+}, Am^{4+}) in $U_{1-y}M_yO_{2\pm x}$ compounds, which nevertheless maintain the fluorite structure. Indeed, we show that the cationic sublattice is basically unaffected by the extreme multi-valence states, whereas complex defects are present in the oxygen sublattice.

[1] CEA, DEN, DMRC, SFMA, LCC, BP 17171, 30207 Bagnols-sur-Cèze, France. [2] Department of Radiation Science and Technology, Faculty of Applied Sciences, Delft University of Technology, 2629JB Delft, The Netherlands. [3] Laboratoire d'Etudes des Microstructures, CNRS-ONERA, 92322 Chatillon, France. [4] European Commission, Joint Research Centre Karlsruhe, P.O. Box 2340, 76125 Karlsruhe, Germany. [5] Laboratory of Theoretical and Applied Physics, University of Sidi Mohamed Ben Abdellah, 30000 Fez, Morocco. [6] Helmholtz-Zentrum Dresden Rossendorf (HZDR), Institute of Resource Ecology, 01328 Dresden, Germany. [7] CEA Cadarache, DEN, DEC, SESC, LM2C, Bat. 151, 13108 Saint-Paul-Lez-Durance, France. [8] DEN-Service de Corrosion et du Comportement des Matériaux dans leur Environnement (SCCME), CEA, Université Paris-Saclay, F-91191 Gif-sur-Yvette, France. [9] Institut fuer Nukleare Entsorgung (INE), Karlsruhe Institute of Technology Campus Nord, 76125 Hermann Von Helmholtz Platz 1, Eggenstein-Leopoldshafen, Germany. Correspondence and requests for materials should be addressed to D.M. (email: Dario.MANARA@ec.europa.eu)

An extensive knowledge of the atomic-scale properties of the nuclear fuel is the first necessary step for understanding and predicting its behaviour in reactor[1]. Uranium dioxide - which crystallises in the FCC fluorite structure (space group $Fm\text{-}3m$), with uranium in $4a$ sites and oxygen in $8c$ - is the most used nuclear fuel worldwide. In oxide fuel-based reactors, $UO_{2\pm x}$ as well as various ternary (or higher order) $U_{1-y}M_yO_{2\pm x}$ solid solutions can be encountered, as fresh fuel (M = Pu), transmutation targets (M = Np or Am) or irradiated fuel (M = fission products, as d-transition metals and lanthanides). These materials originate by substitution of uranium atoms (U^{4+}) with other cations which are not necessarily in a tetravalent state. In these $U_{1-y}M_yO_{2\pm x}$ compounds, which present mostly ionic character, a direct connection exists between the cationic oxidation state and the oxygen stoichiometry, generally indicated with the Oxygen/Metal ratio (O/M ratio). This is a crucial point to understand for the safety assessment of nuclear fuels because their thermal properties, as for instance the melting point and the thermal conductivity, which determine their behaviour in reactors and safety margins, are dramatically affected by changes in the O/M ratio. For this reason, the atomic-scale properties of key $U_{1-y}M_yO_{2\pm x}$ solid solutions have been recently investigated using spectroscopic techniques such as XAS[2–10], NMR[6] and Raman spectroscopy[7,11–13]. For oxygen-stoichiometric (O/M = 2.00) compounds such as $(U,Ce)O_2$[2], $(U,Th)O_2$[14], $(U,Pu)O_2$[3,8] and $(U,Np)O_2$[6], each cation is in the tetravalent state and no oxygen vacancies nor interstitials are observed. The only effect generally observed on the local structure of these mixed dioxides is a variation of the metal-oxygen distance, consistent with the differences in the M^{4+} ionic radii. Non-stoichiometric FCC $(U,Pu)O_{2\pm x}$ oxides were also studied: for O/M<2, Pu^{3+}, Pu^{4+} and U^{4+} coexist and oxygen vacancies are observed;[8] for O/M > 2, the presence of oxygen interstitials is balanced by a partial oxidation of uranium to U^{5+}, whereas plutonium remains tetravalent[3].

The $(U,Am)O_{2\pm x}$ solid solution constitutes a special case, exhibiting unique features in comparison to the other actinide dioxides: XAS measurements reported on oxygen-stoichiometric (O/M = 2.0) $U_{1-y}Am_yO_2$ with $y \le 0.2$ have shown that americium is purely trivalent, while uranium is partially oxidised to the pentavalent state, with very close Am^{3+} and U^{5+} contents[4,5]. This charge compensation mechanism shows similarities with $U_{1-y}Ln_yO_2$ solid solutions bearing trivalent lanthanides, such as $U_{1-y}La_yO_2$[9] and $U_{1-y}Gd_yO_2$[10], even if the mechanism seems insufficient to maintain the oxygen stoichiometry for higher americium content. Indeed, a recent XAS study on an $U_{0.5}Am_{0.5}O_{2-x}$ sample revealed an O/M equal to 1.93(2), with americium still trivalent and an average oxidation state of +4.65(3) for uranium[7]. Moreover, single phase $U_{1-y}Am_yO_{2\pm x}$ oxides have been reported for Am concentrations up to 0.70[15,16], whereas $U_{1-y}Ln_yO_2$ solid solutions exist only for $y \le 0.50$, which represents the limit to the M^{3+}/U^{5+} charge balance. Therefore, questions arise on how $U_{1-y}Am_yO_{2\pm x}$ solid solution can be achieved for [Am] > 0.50, whether Am^{4+} can exist, which is the highest possible oxidation state of uranium in these compounds and whether U^{6+} can be accommodated in a fluorite environment. Furthermore, the crystallographic effects of this unique charge distribution need to be investigated, as they could reveal new peculiarities of the fluorite structure. In order to shed light on these open questions, we combined XRD, XAS and Raman spectroscopy to extend the previous studies to $U_{1-y}Am_yO_{2\pm x}$ with high americium contents. It is also important to point out that such Am-rich compositions have hardly been studied until now, because of their high radioactivity and the scarce availability of these materials.

Results

Cationic charge distribution. $U_{1-y}Am_yO_{2\pm x}$ oxides were synthesised over a large composition domain, for y ranging from 0.075 to 0.67. The formation of single-phase fluorite-type oxides was always confirmed by X-ray diffraction (Supplementary Fig. 1). Specifically, the XRD patterns were systematically checked for the presence of other oxides, such as U_4O_9 (s.g. $I\text{-}43d$[17]), U_3O_8 (s.g. $P\text{-}62m$[18]) or Am_2O_3 ($P\text{-}3m1$[19]), but the characteristic diffraction peaks of these structures were never observed. Moreover, the presence of more than one fluorite phase was excluded: fluorite dioxides which differ in compositions have different lattice parameters and this causes shifts in the characteristic diffraction peaks, which were not observed in this case. Finally, good agreement between data and fits were obtained performing Rietveld refinements with a single fluorite-phase. Thus, these results corroborate the existence of the (U,Am)$O_{2\pm x}$ solid solution for americium contents above 50 mol.%[15,16]. To understand the variation of the electronic structure as a function of the americium content, X-ray Absorption Near Edge Structure (XANES) spectra were collected at the Am-L_{III} and U-L_{III} edges, for five selected compositions with $y = 0.15$, 0.28, 0.48, 0.57 and 0.67. For $y = 0.15$, the results (see Supplementary Tables 1 and 2) confirmed the previous studies by Prieur et al.[4,5] on the same composition, discussed in the introduction. For the new compositions, the results are compared to reference materials in Figs. 1 and 2, showing the absorption spectra and their second derivatives. For the americium, $Am^{4+}O_2$ and an (Am^{3+})-oxalate were respectively adopted as references for the tetravalent and trivalent state, whereas for uranium $U^{4+}O_2$, $(U^{4+}_{1/2}, U^{5+}_{1/2})_4O_9$, $(U^{5+}_{2/3}, U^{6+}_{1/3})_3O_8$ were used[20].

For the Am-L_{III} edge, the white line positions (zero crossing of the first derivative) of all the $U_{1-y}Am_yO_{2\pm x}$ samples are closer to the oxalate reference rather than to AmO_2, which is shifted to higher energies of ≈ 4 eV (see also Supplementary Table 1). However, for the oxides with $y = 0.57$ and 0.67, a broadening and a slight energy increase of the white lines are observed, which indicate a higher oxidation state of americium in these two samples. Quantitative data were obtained by performing linear combination fits of the $U_{1-y}Am_yO_2$ XANES spectra, using those of the reference materials (see also Supplementary Tables 2 and 3) and the results confirmed these preliminary considerations. The americium was purely trivalent for the compositions with $y = 0.28$ and 0.48, but a mixed Am^{3+}/Am^{4+} oxidation states was obtained for the oxides with higher americium contents. For $U_{0.43}Am_{0.57}O_{2-x}$, the molar fractions of Am^{3+} and Am^{4+} are respectively 0.50(2) and 0.07(2), whereas for $U_{0.33}Am_{0.67}O_{2-x}$ they are 0.49(2) and 0.18(2). These results suggest that the maximum possible fraction of trivalent americium that can be accommodated in the fluorite structure is around 50 mol.%.

For the U-L_{III} edge, the white line positions of all the (U,Am)O_2 samples are clearly shifted toward higher energies than those of UO_2. Specifically, $U_{0.62}Am_{0.28}O_{2\pm x}$ is between those of UO_2 and U_4O_9, whereas for the other oxides the white line positions are between those of U_4O_9 and U_3O_8. Moreover, the absorption spectra are more and more broadened by increasing the americium content. These features indicate an increasing oxidation state of uranium with increasing Am/(Am + U) ratio, as confirmed by the linear combination fits and shown in Fig. 3 (see also Supplementary Table 2), in which the obtained average oxidation states of both uranium and americium are compared to the values from the literature. For $U_{0.62}Am_{0.28}O_{2\pm x}$, the best fit of the U-$L_{III}$ edge spectrum was obtained using the UO_2 and U_4O_9 references, where the former is purely tetravalent and the latter has been proved to be an equimolar mixture of U^{4+} and U^{5+}[20]. It can hence be concluded that, also in $U_{0.62}Am_{0.28}O_{2\pm x}$, there is a U^{4+}/U^{5+} mixture and the cationic fractions can be directly obtained by the XANES results: $[U^{4+}] = 0.40$, $[U^{5+}] = 0.32$ and $[Am^{3+}] = 0.28$. For the other
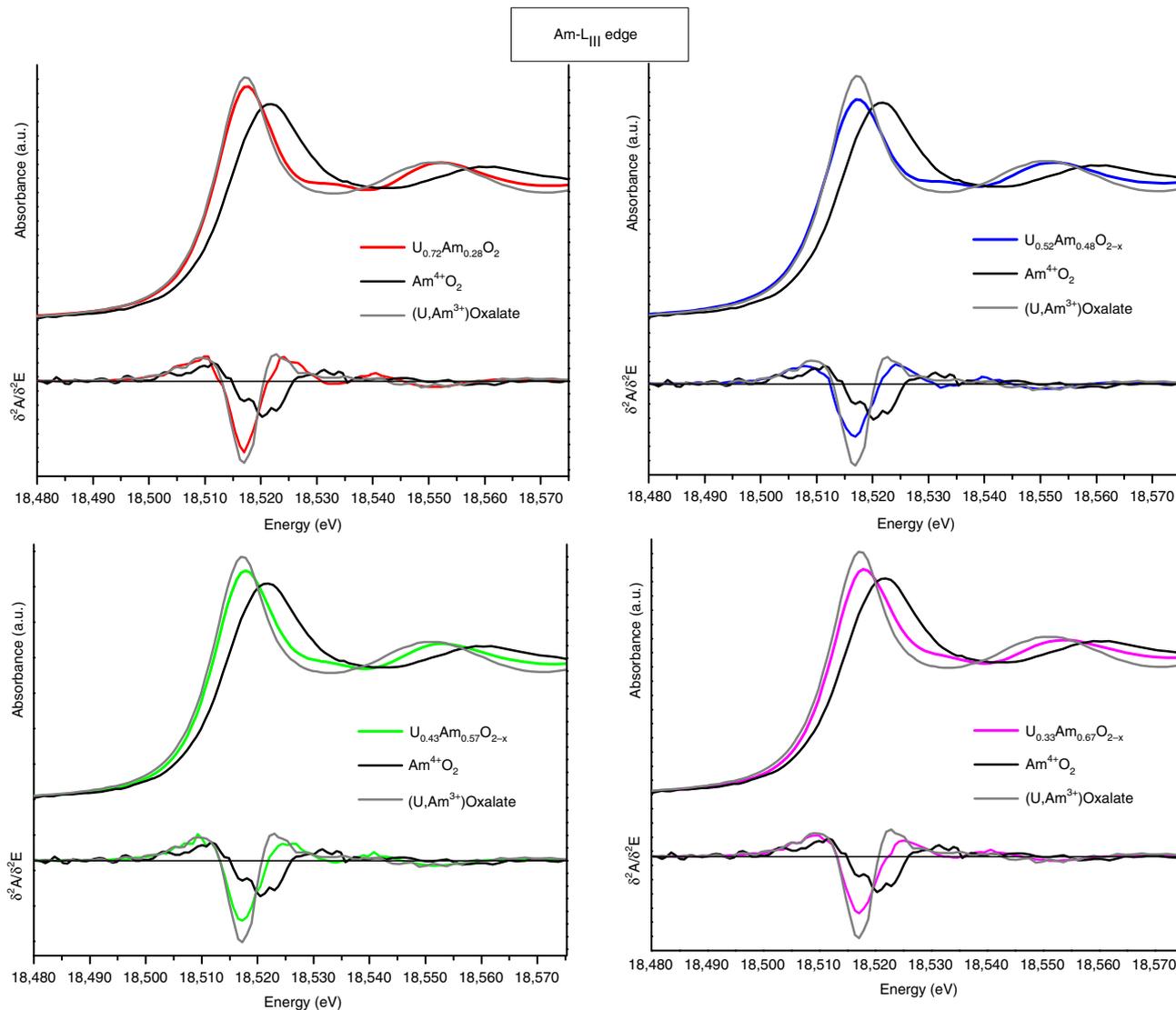
Fig. 1 XANES spectra collected at the L_{III} edge of americium. XANES spectra and their second derivatives for the four $(U,Am)O_2$ oxides are compared to the spectra of the standard compounds

oxides of this work, the best fits were obtained as a linear combination of U_4O_9 and U_3O_8, with the latter showing a mixed U^{5+}/U^{6+} state. In this case, the average oxidation state of uranium can be obtained by the fit and, as shown in Fig. 3, the maximum value of 4.89 is observed for $Am/(Am + U) = 0.67$. However, since the U average oxidation state is strictly lower than 5+, one cannot unambiguously conclude on the presence of U^{6+} from these fits, since two references with mixed oxidation states were used, respectively U^{4+}/U^{5+} and U^{5+}/U^{6+}. Indeed, the ideal case would be to use an oxide reference, with cubic symmetry and pure pentavalent uranium, but the U_3O_8 was selected because it is the only stable uranium oxide with average oxidation state higher than 4.5. In order to further investigate this point and confirm the previous results, complementary HERFD measurements at M_{IV}/M_V edges of uranium and americium were performed on $U_{0.52}Am_{0.48}O_{2-x}$ and the available references. The results are shown in Fig. 4. For Am-M_V, the white line of the mixed oxide is clearly shifted toward lower energy than AmO_2, confirming the reduced state of americium (unfortunately, the trivalent reference was not available). For the U-M_{IV} edge, the spectrum of $U_{0.52}Am_{0.48}O_{2-x}$ is clearly aligned with the U^{5+} contribution of the U_4O_9 spectrum[20], confirming that uranium is almost completely pentavalent in this compound. The U_3O_8 spectrum is instead shift to higher energy

and this indicates that hexavalent uranium is not present in the mixed oxide, as will be further discussed on the basis of the EXAFS data herein.

Oxygen stoichiometry. The O/M ratios, shown in Fig. 3, were computed (from electroneutrality) using the oxidation states of uranium and americium, obtained from the XANES data (see also Supplementary Table 3). The $U_{0.62}Am_{0.28}O_{2.01}$ oxide is almost stoichiometric, with its molar fraction of U^{5+} very close to the americium (purely trivalent), which confirms the charge compensation mechanism previously observed for the mixed oxides with $Am/(Am + U) \leq 0.20$[4,5]. The oxidation of uranium is not sufficient to completely compensate the Am^{3+} content in the Am-U equimolar oxide: the $U_{0.53}Am_{0.47}O_{2-x}$ sample was hypostoichiometric, with an O/M ratio of 1.97(2). Moreover, above this point, the observed O/M ratio decreases with the americium content, passing to 1.93(2) and 1.90(2) for $Am/(Am + U) = 0.57$ and 0.67, respectively. The decrease occurs despite the further oxidation of uranium and the appearance, for the first time, of Am^{4+} in the solid solution. The Am^{3+} content is very close for the three oxides with $Am/(Am + U) \geq 0.48$, suggesting that the maximum content of trivalent americium that can be accommodated in the $(U,Am)O_2$ solid solution is around
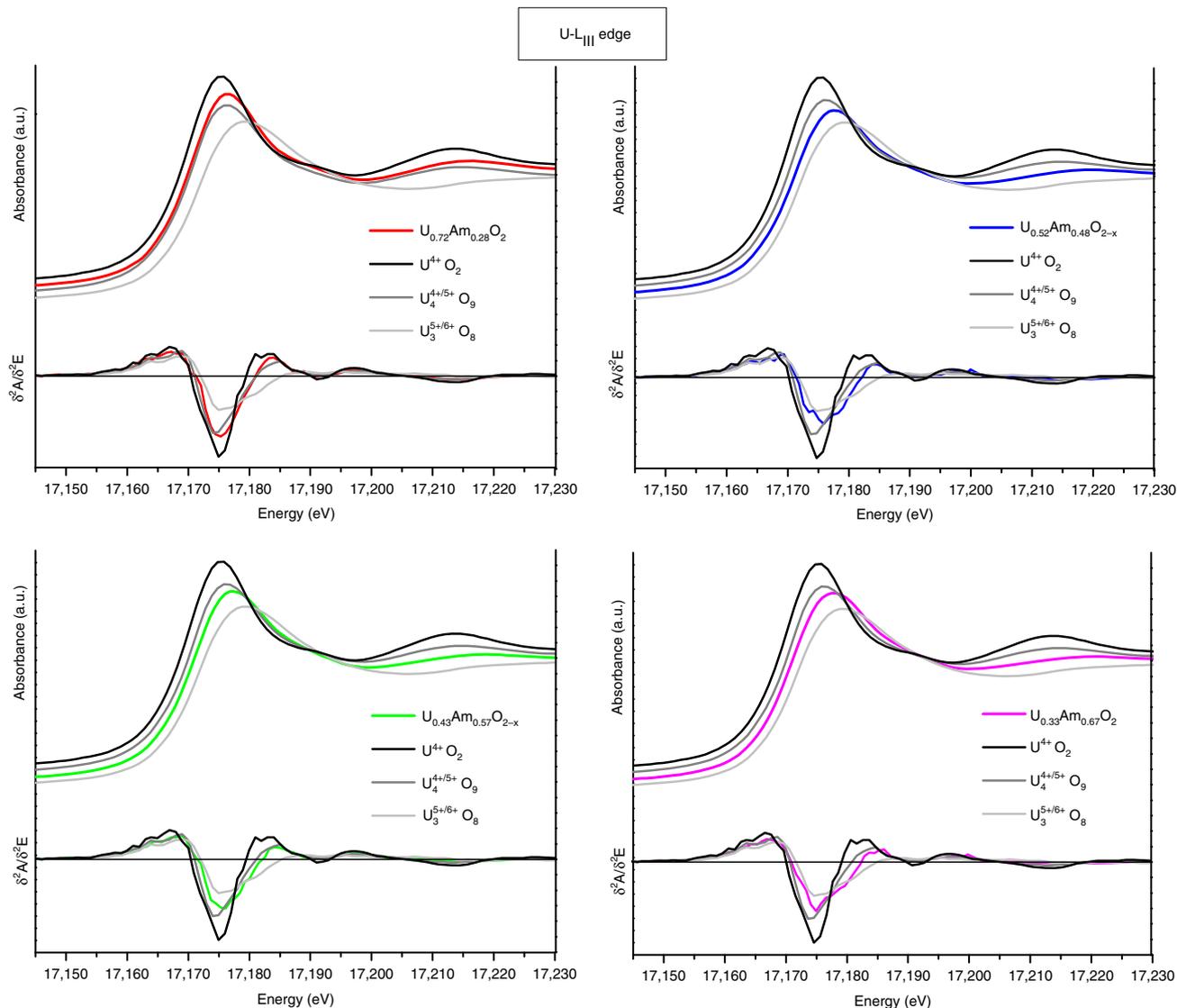
3

Fig. 2 XANES spectra collected at the L_{III} edge of uranium. XANES spectra and their second derivatives for the four (U,Am)O_2 oxides are compared to the spectra of the standard compounds

50 mol.%. Above this value, the americium is partially oxidised to the tetravalent state.

Local structure from EXAFS. The Am L_{III} and U L_{II} EXAFS spectra acquired at 15 K on the four oxides with Am/(Am + U) = 0.28, 0.48, 0.57 and 0.67 are reported in Figs. 5 and 6 respectively, together with their Fourier transforms.

For the Am L_{III} edge, the EXAFS spectra are similar for all the compositions, and the only remarkable difference is a loss of intensity as the americium content increases, indicating most probably a growing disorder. The Fourier transforms of the spectra show two main peaks, the first around 1.9 Å and the second around 3.8 Å. These features are characteristic of the fluorite structure, where the first peak corresponds to the first coordination shell, constituted by 8 oxygen anions, and the second peak is mainly due to the second neighbour shell, constituted by 12 cations. Confirming these qualitative observations, the Am-L_{III} EXAFS data could be very well refined using a fluorite-type structural model for all the four compositions.

For the refinement, the structural parameters obtained by XRD- reported in Table 1 (corrected for the self-irradiation

effects due to the ^{241}Am α-decay[15,21])- were adopted as starting values. The fits were then performed by optimising the interatomic distances R, the number of atoms N in the neighbour shells and the Debye-Waller factors σ^2 of the models. The resulting parameters and the R-factors of the fits are reported in Table 2.

For the first Am-O shell, the distances obtained by EXAFS are considerably larger than those expected by XRD, in agreement with the previous EXAFS data reported in the literature[4,5]. This elongation is consistent with the preferred trivalent state of americium, since the ionic radius of Am^{3+} is larger than that of the other identified cations: $r(Am^{3+}) = 1.09$ Å, $r(Am^{4+}) = 0.95$ Å, $r(U^{4+}) = 1.00$ Å, $r(U^{5+}) = 0.89$ Å[22]. However, a decrease in the Am-O distance is observed for americium contents above 48%, passing from 2.433(5) Å to 2.417(5) and 2.404(5) Å, respectively for Am/(Am + U) = 0.57 and 0.67. This is consistent with the XANES results, that showed only Am^{3+} for Am/(Am + U) up to 0.48, whereas Am^{4+} appeared in the two other compositions. For the first Am-U/Am shell, the distances obtained by EXAFS are slightly lower than those expected by XRD, but within the uncertainty limits. The refined Debye-Waller
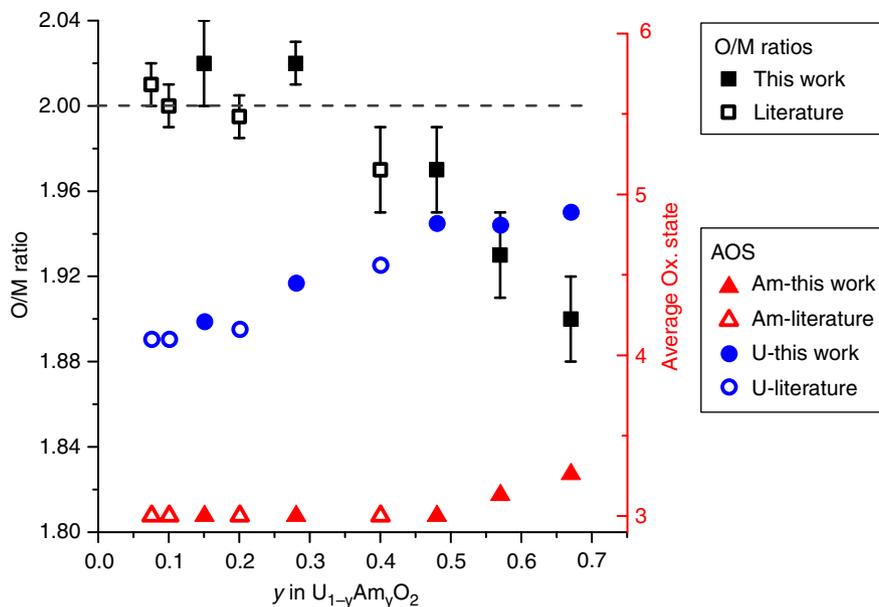
Fig. 3 Compositions of (U,Am)O$_2$ oxides. The O/M ratios are represented on the left axis scale, the average oxidation states (AOS) of U and Am are shown on the right axis scale. The values obtained in this work (full symbols) are compared to the data in the literature (empty symbols)[4,5,7]. The experimental uncertainties are reported for the O/M ratios as error bars
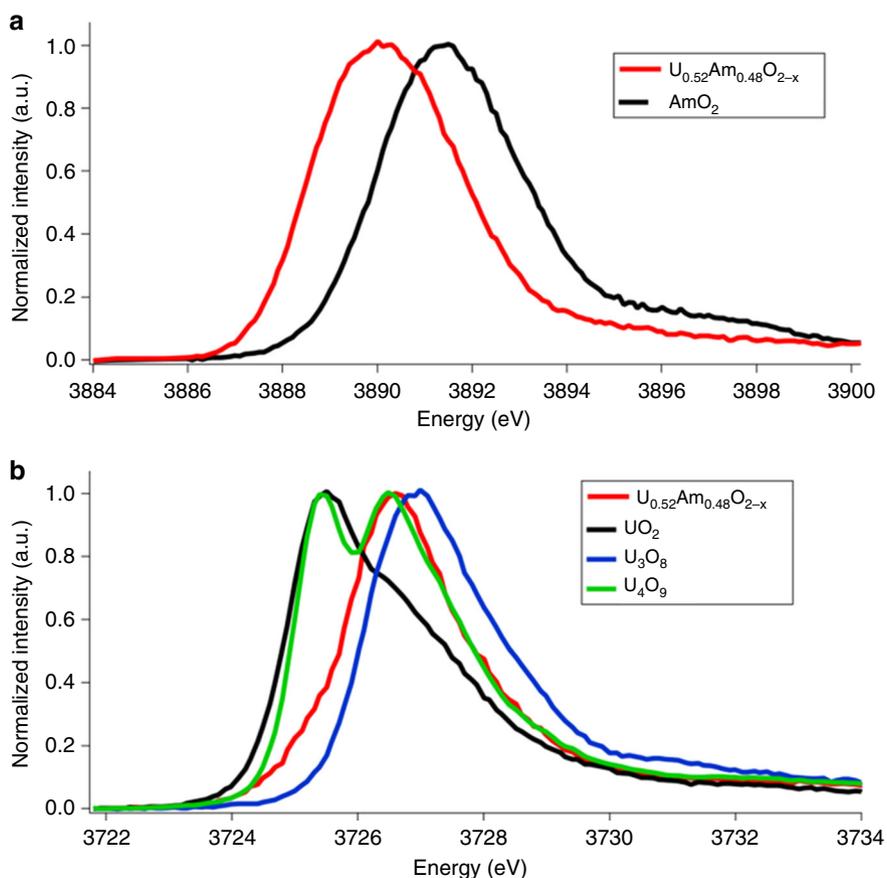
Fig. 4 HR-XANES spectra of U$_{0.52}$Am$_{0.48}$O$_{2-x}$. The spectra collected at the Am-M$_V$ (**a**) and U-M$_{IV}$ (**b**) edges of U$_{0.48}$Am$_{0.52}$O$_{2-x}$ are compared to the reference compounds

factors are generally low because the data were recorded at 15 K. At such temperatures, the thermal contribution can be neglected and the Debye-Waller factors can be attributed only to the structural disorder. The obtained values are always larger for the oxygen shells than for the cation shells, as expected from the higher mobility of oxygen compared to that of uranium/americium. A general increase of the structural disorder is observed by increasing the americium content, as already

$Am\text{-}L_{III}$

a

b

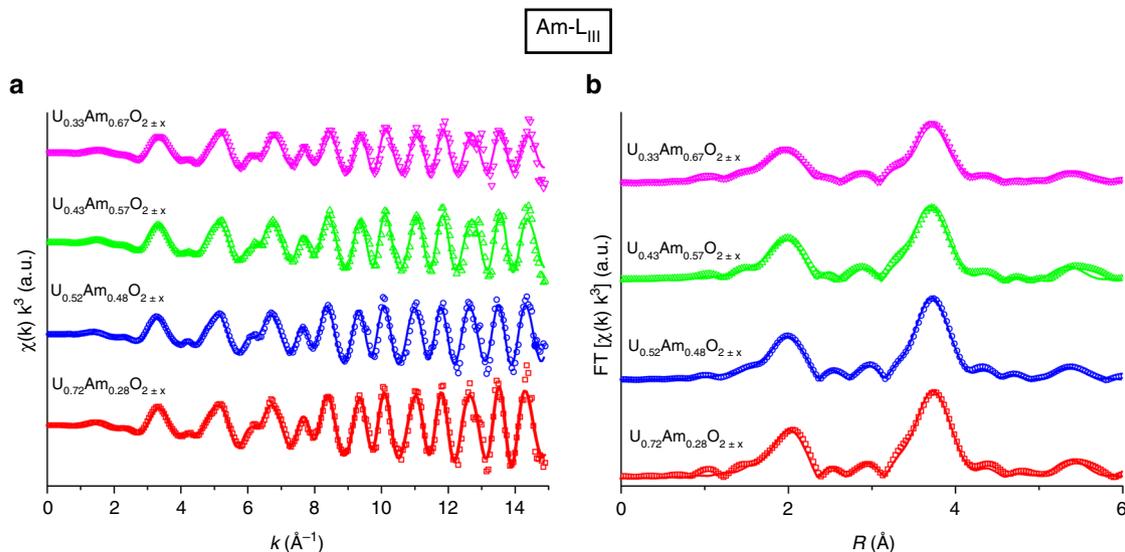**Fig. 5** Am-L_{III} EXAFS data. **a** EXAFS spectra weighted in k^3 and **b** Fourier transforms (FT boundaries 3.5–13.5 Å^{-1}, dk = 2 Å^{-1}). Points: experimental data, lines: fits

$U\text{-}L_{II}$

a

b

Fig. 6 U-L_{II} EXAFS data. **a** EXAFS spectra weighted in k^3 and **b** Fourier transforms (FT boundaries 3.5–11.5 Å^{-1}, dk = 2 Å^{-1}). Points: experimental data, lines: fits

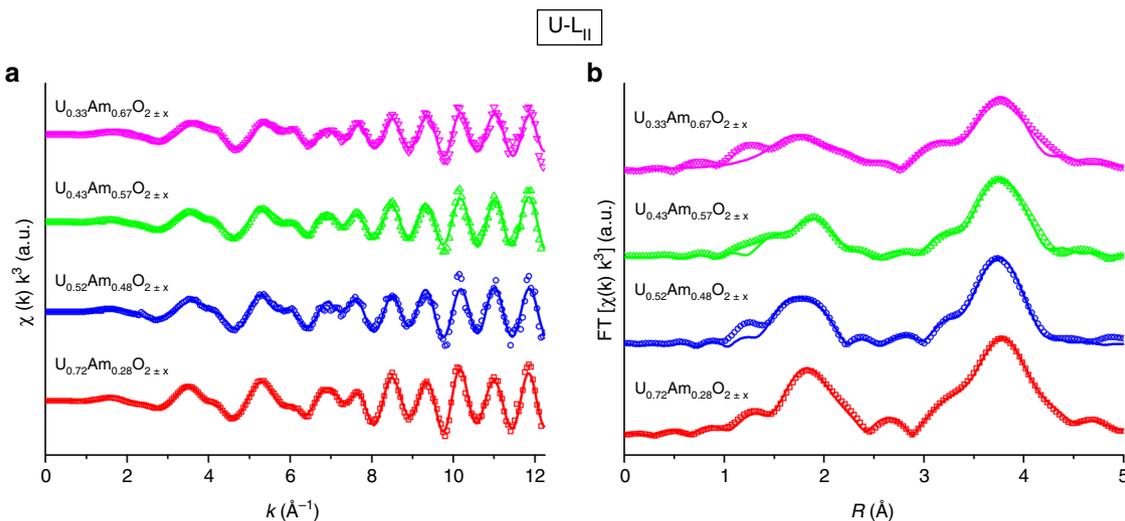**Table 1 XRD lattice parameters and corresponding interatomic distances**

Sample	Lattice parameter (Å)	M-O distance (Å)	M-M distance (Å)
$U_{0.72}Am_{0.28}O_{2.02}$	5.468 (1)	2.368	3.866
$U_{0.52}Am_{0.48}O_{1.97}$	5.466 (1)	2.367	3.865
$U_{0.43}Am_{0.57}O_{1.93}$	5.459 (1)	2.364	3.860
$U_{0.33}Am_{0.67}O_{1.90}$	5.468 (1)	2.360	3.854

mentioned. Finally, the refinement of the coordination numbers around americium did not reveal significant deviations from the defect-free fluorite structure, except for Am/(Am + U) = 0.67, for which the refined coordination numbers for the two oxygen shells are significantly lower than the theoretical ones, indicating the presence of oxygen vacancies around americium.

Contrarily to the Am-L_{III} case, the U-L_{II} EXAFS spectra and their Fourier transforms (Fig. 6) exhibit differences among the various compositions. The U-L_{II} EXAFS spectrum of $U_{0.72}Am_{0.28}O_2$ and the related Fourier transform still present the features of the fluorite structure, whereas the other oxides, in addition to a loss of intensity, show differences in the EXAFS oscillations for k between 1–7 Å^{-1}. These affect the peaks of the Fourier transform at about 1.9 Å, which reveal low intensities and strong broadening. In agreement with this visual observation, the defect-free fluorite structural model fitted only the EXAFS data of $U_{0.72}Am_{0.28}O_{2.02}$ well. The refined U-O distances (Table 2) are, however, considerably shorter both than the value of 2.36 Å reported in the literature for UO_2 and the distances derived from the XRD data. This is consistent with a high molar fraction of U^{5+} as indicated by XANES, since U^{5+} has an ionic radius smaller than U^{4+}. Similarly, to the Am L_{III} edge, the Debye-Waller factors exhibit as expected higher values for the U-O shells than for the U-U/Am shells. Notably, the refined values are

Table 2 Structural data from the refinement of the EXAFS spectra

Sample	Edge	Shell	R (Å)	N	σ^2 (Å^2)	R factor
$U_{0.72}Am_{0.28}O_{2.02}$	Am-L_{III}	O1	2.438 (4)	7.9 (5)	0.0054 (4)	0.009
		Am/U1	3.858 (5)	11.8 (5)	0.0033 (5)	
		O2	4.48 (1)	24	0.014 (3)	
		Am/U2	5.475 (5)	6	0.0031 (4)	
	U-L_{II}	O1	2.330 (6)	8.1 (5)	0.0094 (4)	0.007
		Am/U1	3.860 (5)	11.9 (5)	0.0041 (2)	
		O2	4.517 (8)	24	0.009 (1)	
		Am/U2	5.45 (1)	6	0.006 (1)	
$U_{0.52}Am_{0.48}O_{1.97}$	Am-L_{III}	O1	2.433 (5)	7.9 (5)	0.0062 (4)	0.006
		Am/U1	3.855 (5)	11.9 (5)	0.004 (1)	
		O2	4.47 (1)	24	0.014 (2)	
		Am/U2	5.47 (1)	5 (1)	0.005 (1)	
	U-L_{II}	Ocubo1	2.183 (5)	1.7 (5)	0.004 (1)	0.017
		Ofluo1	2.359 (5)	5.4 (5)	0.008 (2)	
		Ocubo2	2.87 (1)	1.7 (5)	0.021 (2)	
		Am/U1	3.85 (1)	12	0.004 (1)	
		Ofluo2	4.52 (1)	22 (3)	0.012 (1)	
$U_{0.43}Am_{0.57}O_{1.93}$	Am-L_{III}	O1	2.417 (8)	8	0.0072 (7)	0.02
		Am/U1	3.836 (5)	12	0.0042 (2)	
		O2	4.45 (4)	24	0.014 (3)	
		Am/U2	5.46 (1)	6	0.004 (2)	
	U-L_{II}	Ocubo1	2.172 (5)	1.5 (5)	0.004 (1)	0.018
		Ofluo1	2.340 (5)	5.4 (5)	0.007 (2)	
		Ocubo2	2.84 (1)	1.5 (5)	0.001 (1)	
		Am/U1	3.86 (1)	12	0.0038 (8)	
		Ofluo2	4.42 (1)	22 (3)	0.011 (1)	
$U_{0.33}Am_{0.67}O_{1.90}$	Am-L_{III}	O1	2.404 (6)	7.3 (5)	0.0092 (6)	0.011
		Am/U1	3.837 (5)	12	0.0053 (2)	
		O2	4.42 (1)	22 (2)	0.012 (2)	
		Am/U2	5.45 (2)	6	0.006 (3)	
	U-L_{II}	Ocubo1	2.17 (1)	1.7 (5)	0.009 (1)	0.03
		Ofluo1	2.29 (1)	5.4 (5)	0.012 (1)	
		Ocubo2	2.82 (1)	1.7 (5)	0.008 (1)	
		Am/U1	3.85 (1)	12	0.0046 (8)	
		Ofluo2	4.404 (1)	22 (3)	0.011 (1)	

The parameters without uncertainty were fixed during the fit

higher than those reported for UO_2 at the same temperature[7], indicating again an increase in the structural disorder with the americium substitution.

For the other oxides with americium contents $y \geq 0.48$, the attempt to fit the EXAFS data using a defect-free fluorite structural model gave poor results, failing in particular to reproduce the $1 \leq k \leq 7$ Å^{-1} region of the EXAFS spectra and the peak in the $1.3 \leq R \leq 2.8$ Å domain of the Fourier transform. The broadening of this peak is similar to the U-L_{III} EXAFS data of the U_4O_9[7] (Supplementary Fig. 2). For this reason, various structural models based on UO_{2+x} and U_4O_9 polymorphs[17,23–26] were tested for the refinement of the EXAFS data and a good result was obtained with one based on the "average" β-U_4O_9 structure (*F-43m*), proposed by Cooper and Willis[17]. In this structure, the cations and most of the O atoms are located at fluorite-type positions, but the fluorite-type oxygen sublattice (Ofluo in Table 2) shows a significant proportion of vacancies, whereas two additional interstitial positions are available for oxygen: the 48(h) ($x = y = 0.617$ and $z = 0.5$) and the 16(e) ($x = y = z = 0.608$) Wyckoff positions. However, since the 16(e) position has a very low occupancy (0.010), only the 48(h) interstitial oxygen atoms were included in the EXAFS model (Ocubo in Table 2).

The main effect of including these cuboctahedral interstitials is the appearance of two additional U-O distances: one at about 2.20 Å and the other at about 2.87 Å, hence respectively shorter and longer than the U-O_{fluo} distance.

Using this structure, the EXAFS data of both the U_4O_9 reference (Supplementary Fig. 2) and the $U_{1−y}Am_yO_{2−x}$ oxides with $y \geq 0.48$ were well fitted, providing the parameters reported in Table 2. This proves the presence of oxygen vacancies in the normal fluorite sites and of oxygen interstitial atoms in cuboctahedral sites for these $(U,Am)O_{2−x}$ oxides. However, interesting differences compared to U_4O_9 can be noticed. First, for the three $(U,Am)O_2$ samples, the number of oxygen atoms in the fluorite position, equal to 5.4(5), is lower than that of U_4O_9, equal to 6.3(5), whereas the number of atoms in the interstitial positions are identical (within the uncertainty). This indicates a higher concentration of oxygen vacancies, well in line with its hypostoichiometric composition (O/M < 2) in comparison to U_4O_9. Second, the first U-O_{cubo} distance of the mixed $(U,Am)O_{2−x}$ (2.17 to 2.18 Å) is significantly shorter than that observed for U_4O_9 (2.248(5) Å). This is likely due to the average oxidation state of uranium, which is higher in the $(U,Am)O_{2−x}$ oxides than in U_4O_9, as seen in the previous section. Note, however, that the obtained U-O distances are, in any case, considerably larger than the uranyl U^{+6}-O distance of ≈1.8 Å observed in U_3O_8[27] or UO_3[28]. This confirms the absence of hexavalent uranium, as previously indicated by the HERFD data.

Raman spectroscopy. The Raman spectra shown in Fig. 7 were obtained on $U_{1−y}Am_yO_{2±x}$ oxides, with $0.075 < y < 0.67$, using an excitation wavelength $\lambda = 647.5$ nm. For all the compositions, the
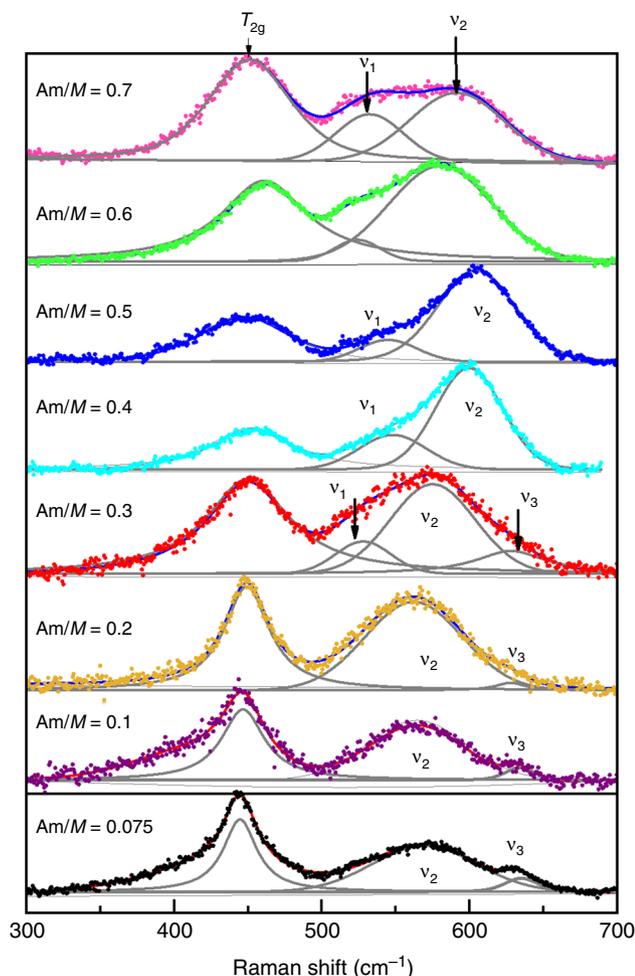
Fig. 7 Raman spectra of (U,Am)O$_{2\pm x}$ oxides. The experimental Raman spectra are shown as coloured points, the Lorentzian functions used to deconvolute the spectra and their sum are represented with solid lines

spectra reveal a first symmetric band, at wavenumber around 450 cm^{-1}, and a large envelope, likely including 2–3 modes, between 500 and 650 cm^{-1}.

For symmetry reasons, only one triply degenerative T$_{2g}$ Raman active mode[29] is allowed by the Factor Group Theory for the fluorite structure. This mode is originated from the M–O stretching, with M being coordinated in a cubic environment of eight oxygen atoms. The presence of forbidden modes in the Raman spectra of U$_{1-y}$Am$_y$O$_{2\pm x}$ oxides is not surprising; it has already been observed in various UO$_2$[30–33], U-Actinide[34] and U-rare earth dioxides[11,13], as a result of breaks in the translational symmetry, which can be induced by different factors, namely irradiation, doping, reduction or oxidation.

The observed changes in the Raman spectra of Fig. 7 can be summarised as follows: (1) a non-linear shift and broadening of the T$_{2g}$ with the Am content; (2) non-linear shift of the envelope centred at 560 cm^{-1} and (3) continuous changes in the relative intensities. A detailed band-profile analysis was carried out.

As can be seen in Fig. 8a, the T$_{2g}$ mode initially upshifts until 40% Am and then drops in frequency at $y = 0.48$. At this particular point, the band begins to substantially move towards higher wavenumbers, reaching the value of 461 cm^{-1} for U$_{0.43}$Am$_{0.57}$O$_{1.93}$ and then downshifts for U$_{0.33}$Am$_{0.67}$O$_{1.90}$. Similarly, the bandwidth of this mode generally increases with the americium content; at 48% Am it presents a maximum of

broadening and then tends to stabilise at a lower value for the remaining compositions.

The T$_{2g}$ band is assigned to the antisymmetric breathing of eight oxygen atoms around the central cation (U/Am). Thus, its position and FWHM are highly affected by the M–O bond strength and the local order of the oxygen sub-lattice. The initial upshift of the T$_{2g}$ frequency up to Am/M = 0.40 implies a gradual increase in the bond strength, which is likely fostered by the partial oxidation of uranium to U^{5+}. The gradual broadening of the band for this composition range can be ascribed to the increase of the americium content, which results in a progressive disorder in the U/Am cation statistical distribution in the lattice, which then enhances the broadening of the U/Am-O vibration.

The loss of regularity in the T$_{2g}$ variation for Am/M > 0.40 could be expected from the complex situation highlighted by the XANES/EXAFS results and is not trivial to interpret. Various factors contribute simultaneously to modify the M–O bond strength, namely the departure from the oxygen stoichiometry (for Am/(U + Am) > 0.48), the increase of U^{5+} concentration, the appearance of the Am^{4+} (for Am/M ≥ 0.58) and the partial rearrangement of the oxygen atoms in cuboctahedral clusters.

The broad band at higher wavenumbers i.e., 500–650 cm^{-1} was deconvoluted in bands indicated as ν_1, ν_2, ν_3, using Lorentzian functions, and the relative intensities of these three bands as a function of the Am content are shown in Fig. 8b.

The ν_1 band, ranging from 535(5) to 555(5) cm^{-1}, appears only for compositions containing high Am content (Am/M ≥ 0.28), with an almost constant intensity. In literature, this mode was observed in several U$_{1-y}$Ln$_y$O$_{2-x}$ oxides, where Ln is a trivalent lanthanide[11,13]. The authors suggested that this mode originates from an M-O stretching (M = actinide or lanthanide), with M coordinated in a M–O$_{8-x}$ cubic environment with at least one oxygen vacancy. According to this hypothesis, the ν_1 mode can be seen as a Raman signature of oxygen vacancies. Therefore, this indicates that the addition of americium higher than ≈30% leads to abundant formation of oxygen vacancies, in agreement with the EXAFS results.

The ν_2 band, at about 575 cm^{-1}, is present for all the compositions and its intensity increases with the americium content. This band can be associated to the forbidden LO (longitudinal optical) mode, which was reported several times for actinide dioxides and whose origin has been debated for long[30,31,35,36]. Livneh and Sterer[31] finally showed that the activation of the LO modes occurs via a resonance process and hence it depends on the difference between the energy of the laser and the band gap in the investigated material. This latter is equal to 2–2.5 eV for UO$_2$[37–40] whereas a lower value of 1.3 eV was measured for AmO$_2$[41]. Thus, the increase in the intensity of this mode for 0.075 ≤ Am/(Am + U) ≤ 0.40 is a result of the band gap contraction induced by the increase of the Am content. However, above 40% Am, a jump in the intensity of this mode occurred, followed by a strong decrease. This behaviour is plausible when the energy of the laser, i.e., 1.9 eV becomes higher than the band gap and thus the resonance conditions are not met anymore.

The ν_3 band has been observed for compositions with Am/(Am + U) ≤ 0.30 at an almost constant position of about 632 cm^{-1}. This band was observed several times in UO$_{2+x}$ and U$_4$O$_9$ oxides[32] and it has been attributed to vibration modes involving oxygen atoms in cuboctahedral clusters.

It can be surprising that the ν_3 band was observed for the compositions with low Am content, since the EXAFS results revealed the presence of oxygen interstitials around uranium only for Am/(Am + U) ≥ 0.48. However, this mode was often observed in initially stoichiometric UO$_2$ because of a surface oxidation induced by the laser. A similar phenomenon is likely at the origin
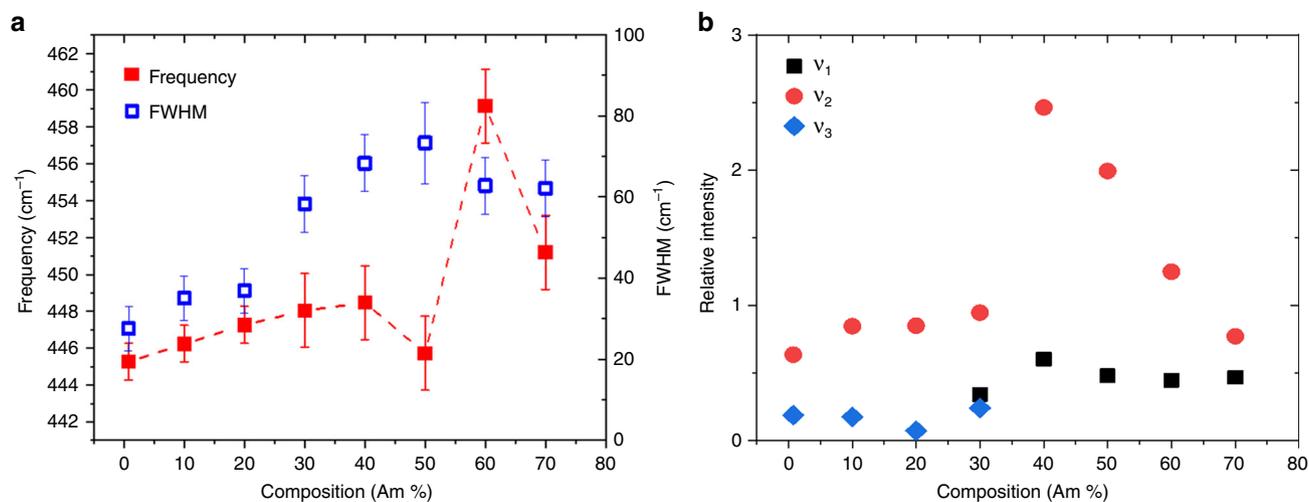
Fig. 8 Raman data analysis. **a** Wavenumber (red) and Full Width at Half Maximum (blue) of the T_{2g} mode, together with the experimental uncertainties (error bars), in $U_{1-y}Am_yO_{2\pm x}$ oxides. **b** Relative intensities of the ν_1, ν_2, ν_3 bands (normalisation to the T_{2g} intensity)

of the ν_3 band of the (U,Am)O_2 oxides with Am/(Am + U) $\leq$ 0.30, whereas a surface oxidation can be excluded for the (U,Am) O_2 oxides with higher Am/(Am + U), since the americium stabilises the solid solution with regard to an O/M increase[42]. It can also be surprising that for $0.4 \leq$ Am/(Am + U) ≤ 0.68 this mode is not any longer visible, since the U-L_{II} EXAFS spectra have shown a progressively distorted oxygen sublattice. It must be kept in mind that EXAFS is an element-selective technique, whereas Raman spectroscopy probes simultaneously the U–O and Am–O vibrations. It is true that the oxygen sublattice around uranium is affected by increasing the americium content, but simultaneously the total amount of uranium diminishes. Therefore, the main contribution to the Raman spectrum intensity comes from the Am-O stretching. Since the sublattice around americium is not affected by oxygen interstitials, Raman spectroscopy sees a more ordered sample as a whole.

Discussion

The first XAS studies performed by Prieur et al.[4,5] on $U_{1-y}Am_yO_{2\pm x}$ oxides, with y up 0.20, highlighted that the formation of this fluorite-type solid solution occurs in a peculiar way. Indeed, the simultaneous presence of Am^{3+}, U^{4+} and U^{5+}, was shown by XANES, contrarily to the other actinide dioxide solid solutions, where only cationic couples (An^{3+}/An^{4+} or An^{4+}/An^{5+}) co-exist. Moreover, the oxygen stoichiometry close to 2.00 and the similar Am^{3+}-U^{5+} molar fractions suggested a charge compensation mechanism. Our study shows that this mechanism can be extended to Am/(Am + U) up to about 30 mol.%. In the $U_{0.72}Am_{0.28}O_{2.01}$ oxide here studied, the americium was purely trivalent and a high average oxidation state (+4.45) was found for the uranium, corresponding to a U^{5+} fraction of $\approx$30%. Similar to the investigations of Prieur et al.[4,5], the EXAFS data did not reveal remarkable changes of the local structure for this oxide, with the exception of a shortening of the U-O distance and a lengthening of the Am-O distance.

The effects become instead more and more important by increasing the americium content in the solid solution. In agreement with the study of Lebreton et al.[7] on $U_{0.6}Am_{0.4}O_{1.98}$ and $U_{0.5}Am_{0.5}O_{1.94}$, our investigation of $U_{0.52}Am_{0.48}O_{1.98}$ revealed important changes in the oxygen sublattice around uranium, including both vacancies in the normal fluorite sites and interstitials in cuboctahedral positions, similar to U_4O_9 polymorphs. These arrangements are possible thanks to the high

average oxidation state of uranium, which increases with the americium content, reaching a value of +4.82(5), even higher than that in U_4O_9 and U_3O_7. This was also clearly confirmed by complementary data collected at the M_{IV} edge of uranium. However, this is not sufficient to compensate for the purely trivalent state of americium: all the investigated samples with $0.4 \leq$ Am/(Am + U) ≤ 0.5 were hypostoichiometric (O/M < 2.0).

The study of the (U,Am)O_2 solid solution was here extended for the first time to compositions with $y > 0.5$. The oxygen stoichiometry kept decreasing with the americium content, with O/M equal to 1.93(2) and 1.90(2), respectively for $U_{0.43}Am_{0.57}O_{1.93}$ and $U_{0.33}Am_{0.67}O_{1.90}$. This decrease of the O/M ratio occurs despite the high oxidation state of uranium (maximum value = + 4.89 for Am/(Am + U) = 0.7) and the appearance, for the first time, of tetravalent americium in the mixed oxides. Therefore, the XANES results suggest that the maximum possible molar fraction of Am^{3+} is about 50%; above this value, partial Am oxidation to Am^{4+} appears. Once again, this complicated cationic charge distribution occurs without losing the overall fluorite symmetry. More specifically, the drastic changes in the oxygen sublattice around uranium are accentuated, but the local structure around americium is marginally affected. For the latter, only a shortening of the average Am–O distance (due to the smaller Am^{4+} ionic radius) and a slight increase of the Debye-Waller factors were revealed by EXAFS. Besides, the overall short-range order of the samples was also confirmed by the present Raman spectroscopy results, which showed a decrease in the intensity of the defect bands for Am/(Am + U) = 0.6 and 0.7. This is consistent with the fact that the main contribution to the Raman signal, for these samples, come from americium (more abundant than uranium), which preserves its local order.

It must be stressed that the results herein shown cannot be explained by the presence of more than one phase, as one could wonder from the observation of multiple oxidation states in the samples. Indeed, if this hypothesis is considered, the high average oxidation state of uranium should imply elevated contents of phases such as U_4O_9 and U_3O_8. For instance, in $U_{0.33}Am_{0.67}O_{1.90}$, these phases should represent a total fraction of $\approx$30 wt.% and the remaining 70 wt.% should be constituted by AmO_{2-x}. Such a configuration should be clearly detectable by XRD: first, the U_3O_8 present a hexagonal symmetry, completely different than the fluorite; second, structures as U_4O_9 and AmO_{2-x}, even if both cubic, have different lattice parameters- 5.450(1) Å for U_4O_9 and 5.390 Å for AmO_2 (at the saturation of the self-irradiation

swelling), which imply clear shifts in the XRD characteristic reflections and hence the possibility to discern the two phases. None of this has been shown by our XRD data, confuting the hypothesis of secondary phases in the sample, if non in negligible contents. Moreover, it is known that AmO_{2-x} is not stable at room temperature and it rapidly re-oxidises to $AmO_{2.0}$, hence the presence of Am^{3+} can be explained only by the solid solution formation. Therefore, the ensemble of the results here presented indicate the presence of one phase, the $(U,Am)O_{2\pm x}$ solid solution, in which the cations occupy regular fluorite sites, while the oxygen sublattice is affected by the aliovalent configuration.

In conclusion, unique electronic and local structures were shown in this study for the $U_{1-y}Am_yO_2$ solid solution, in which extreme multi-valence states can be observed. Besides the interest for the use of these materials as transmutation targets, the results of this work show also new general features of the fluorite structure. Here we clarify that the fluorite order can be maintained even with the presence of four different cationic species and even with an almost complete oxidation of uranium to the pentavalent state. The average oxidation state of uranium in the $U_{0.33}Am_{0.67}O_{1.90}$ oxide, equal to +4.48, is the highest ever observed in fluorite-related structures, even higher than in U_3O_7. This structural stability of the fluorite-like symmetry in the dioxide nuclear fuel even under the present conditions is a positive observation in terms of nuclear fuel safety. Moreover, for the first time, we proved that the cuboctahedral oxygen clusters can be formed even in oxygen-hypostoichiometric fluorite structures. These unique features could affect not only the $U_{1-y}Am_yO_{2\pm x}$ oxides, but also other UO_2-based fluorite solid solutions, as for instance those originating from the accommodation of fission products in the reactor and hence could be crucial for a more thorough understanding of the fuel behaviour.

Methods

Sample preparation. $U_{1-y}Am_yO_{2\pm x}$ pellets were manufactured in the hot cells of the Atalante facility, at CEA Marcoule. $UO_{2.04}$ and AmO_2 powders – whose characteristic are detailed in ref. [42][43]– were used as precursors. The former was a batch of depleted uranium dioxide, whose total content of impurities was below 100 ppm. The O/U ratio, equal to 2.04, was measured by polarography. The AmO_2 batch came from a test of liquid–liquid extraction from spent fuel with the EXAM process[44], performed at CEA-Marcoule, and it presented some percent of impurities, mainly Ce (1.7(5) wt.%), Nd (0.5(1) wt.%) and Np (0.4 wt.%). The O/M could not be directly measured, but a thermal treatment under dry air was performed on the AmO_2 powder, at 400 °C for 12 h, which is considered sufficient to establish the stoichiometry $O/Am = 2.0$[45]. The precursor powders were mixed with the nominal compositions Am/M = 10, 15, 30, 50, 60 and 70 mol.%, ground and pressed into pellets of about 500–700 mg. The UMACS powder metallurgy process[46] was applied for the synthesis of the mixed oxides. This includes two thermal treatments- intermediated by a grinding and a re-pelletization- performed in a tungsten furnace, with plateau temperatures of 2023 K, for Am/M ≤30 mol.%, and 1873 K for higher Am concentrations. The atmosphere was composed by flowing Ar/H$_2$(4%) and Ar/O$_2$(1000 ppm), mixed in order to obtain oxygen potentials equal to −450 kJ/mol at 2023 K and −440 kJ/mol at 1873 K. After the synthesis, Thermal Ionization Mass Spectrometry was used to determine the quantity of U and Am in the samples and therefore the obtained Am/(Am + U) ratios. Small fragments of the pellets (~30–50 mg) were used for the Raman spectroscopy study, using the airtight sample holder described in ref. [12]. Manually ground powders were used for XRD (≈40 mg) and XAS (≈1 mg). For this latter, the sample was diluted in 15 mg of boron nitride and confined in two independent sealed holders.

XRD. For the compositions with $y = 0.10$, 0.15, 0.28, 0.48, XRD characterisations were performed at the Atalante facility, using a Bruker D8 X-ray diffractometer in θ–θ Bragg Brentano geometry, specially equipped for radioactive materials. For the compositions with $y = 0.57$ and 0.67, XRD characterisations were performed at the LEFCA facility of CEA Cadarache, using a Bruker D8 Advance X-ray diffractometer in θ–θ Bragg Brentano geometry, completely implemented in a nitrogen flushing glove box. Both the diffractometers are equipped with a copper source (Kα_1 + Kα_2 radiation). Diffraction patterns were recorded in the $25 \leq 2\theta \leq 120°$ range, with a step of 0.01°. Rietveld refinements of the XRD patterns were performed using the FullProf Suite software[47].

XAS. The XAS spectra at U and Am L-edges were recorded at the ROBL beamline at the ESRF (Grenoble, France) under dedicated operating conditions (6.0 GeV, 180 mA). Measurements were performed at room temperature and at 15 K, using for the latter a closed-cycle helium cryostat. Spectra were collected at the Am-L$_{III}$ (18,510 eV), U-L$_{III}$ (17,166 eV) and U-L$_{II}$ (20,948 eV) edges in both transmission and fluorescence modes, using ionization chambers filled with N$_2$/Ar and a Canberra energy-dispersive 13-element germanium solid state detector. A double Si(111) crystal monochromator was used for energy selection and the calibration was performed using metallic foils, namely yttrium (17,038 eV), zirconium (17,998 eV) and molybdenum (20,000 eV). The references were measured at the same time as the samples, in transmission mode, using a third ionization chamber behind the foil.

The HERFD spectra at U-M$_{IV}$ and Am-M$_V$ edges were collected at the ACT end-station of the CAT-ACT beamline at the KARA synchrotron facility (Karlsruhe, Germany)[48]. Measurements were collected at room temperature using the emission spectrometer available at ACT and equipped with five spherically bent Si(110) crystals analysers with 1 m bending radius and focused onto a single diode VITUS Silicon Drift Detector (KETEK, Germany). A gastight box, enclosing the spectrometer and the sample, maintaining constant He atmosphere during all measurements was installed to minimise intensity losses. The incoming X-Ray beam was monochromatized by a Si(111) double crystal monochromator (DCM). The HERFD spectra were obtained by recording the maximum intensity of the U M$_\beta$ (3.3365 keV) or Am M$_\alpha$ (3.4427 keV) emission lines by aligning the 5 crystals at 75.40° and 69.81°, respectively. The sample, crystals and detector were arranged in five vertical Rowland circles intersecting at the sample surface and the detector entrance window. The energy calibration was performed by systematically collecting prior to each (U,Am)O$_2$ samples, a HERFD spectra on UO$_{2.00}$ and Am$_{2.00}$ reference materials mounted on the same sample holder.

The XANES/HERFD spectra have been normalised using linear functions for pre- and post- edge modelling. The white-line maxima have been taken as the first zero-crossing of the first derivative. Pre-edge removal, normalisation and self-absorption correction were performed using the ATHENA software[49]. XANES spectra were compared to data collected on reference materials. For uranium, $U^{4+}O_{2.0}$, $(U_{0.5}^{4+},U_{0.5}^{5+})_4O_9$ and $(U_{2/3}^{5+},U_{1/3}^{6+})_3O_8$ were used. For americium, $Am^{4+}O_2$ and an (Am^{3+})-oxalate were adopted. The XANES spectra of the mixed oxides were fitted by linear combination of the reference materials, between −20 eV and +30 eV in relation to the white line position, using the ATHENA software[49]. From these fits, the average oxidation states of Am and U were derived.

The EXAFS oscillations were extracted from the raw data with the ATHENA software[49] and Fourier-transformed using a Hanning window. Interatomic scattering path phases and amplitudes were calculated with the FEFF 8.40 ab initio code[49]. The ARTEMIS software[49] was used for curve fitting in k^3. For both U and Am shells, the S_0^2 value was initially set at 0.90, while the shift in the threshold energy, the interatomic positions, the Debye-Waller factors and the coordination numbers were fitted. Once the fit reached a satisfactory result, the S_0^2 value was let free to vary and the variations from the initial value were limited.

Raman spectroscopy. Micro-Raman spectroscopy was performed at the European Commission's Joint Research Centre of Karlsruhe, Germany. The experimental set-up was previously described in ref. [12]. An air-tight Raman sample holder was used for the radioactive sample. The excitation source was a Kr + Coherent CW laser operating at a wavelength of 647 nm. The spectrograph was calibrated on a daily basis prior to measurements using the T$_{2g}$ excitation of a silicon single crystal[50], set at 520.5 cm^{-1}.

Data availability

The authors declare that the main data supporting the findings of this study are available within the article and Supplementary Information file. Other relevant data are available from the corresponding author upon reasonable request.

References

1. Konings, R. J. M., Wiss, T. & Beneš, O. Predicting material release during a nuclear reactor accident. *Nat. Mater.* **14**, 247–252 (2015).
2. Martin, P. et al. A XAS study of the local environments of cations in (U, Ce) O$_2$. *J. Nucl. Mater.* **312**, 103–110 (2003).
3. Martin, P. et al. XAS study of $(U_{1-y}Pu_y)O_2$ solid solutions. *J. Alloy. Compd.* **444–445**, 410–414 (2007).
4. Prieur, D. et al. Local structure and charge distribution in mixed Uranium–Americium oxides: effects of oxygen potential and Am content. *Inorg. Chem.* **50**, 12437–12445 (2011).
5. Prieur, D. et al. Accommodation of multivalent cations in fluorite-type solid solutions: case of Am-bearing UO2. *J. Nucl. Mater.* **434**, 7–16 (2013).

6. Martel, L. et al. Structural investigation of Uranium–Neptunium mixed oxides using XRD, XANES, and 17O MAS NMR. *J. Phys. Chem. C* **118**, 27640–27647 (2014).

7. Lebreton, F. et al. Peculiar behavior of $(U,Am)O_{2-\delta}$ compounds for high americium contents evidenced by XRD, XAS, and Raman Spectroscopy. *Inorg. Chem.* **54**, 9749–9760 (2015).

8. Vigier, J.-F. et al. Structural investigation of $(U_{0.7}Pu_{0.3})O_{2-x}$ mixed oxides. *Inorg. Chem.* **54**, 5358–5365 (2015).

9. Prieur, D. et al. Aliovalent cation substitution in UO_2: electronic and local structures of $U_{1-y}La_yO_{2\pm x}$ solid solutions. *Inorg. Chem.* **57**, 1535–1544 (2018).

10. Bès, R. et al. Charge compensation mechanisms in $U_{1-x}Gd_xO_2$ and $Th_{1-x}Gd_xO_{2-x/2}$ studied by X-ray Absorption Spectroscopy. *J. Nucl. Mater.* **489**, 9–21 (2017).

11. Desgranges, L. et al. Miscibility gap in the U–Nd–O phase diagram: a new approach of nuclear oxides in the environment? *Inorg. Chem.* **51**, 9147–9149 (2012).

12. Naji, M. et al. An original approach for Raman spectroscopy analysis of radioactive materials and its application to americium-containing samples. *J. Raman Spectrosc.* **46**, 750–756 (2015).

13. Talip, Z. et al. Raman and X-ray studies of uranium–lanthanum-mixed oxides before and after air oxidation. *J. Am. Ceram. Soc.* **98**, 2278–2285 (2015).

14. Hubert, S., Purans, J., Heisbourg, G., Moisy, P. & Dacheux, N. Local structure of actinide dioxide solid solutions $Th_{1-x}U_xO_2$ and $Th_{1-x}Pu_xO_2$. *Inorg. Chem.* **45**, 3887–3894 (2006).

15. Lebreton, F. *Synthèse Et Caractérisation D'oxydes Mixtes D'uranium Et D'américium*. PhD dissertation, Université de Limoges (2014).

16. Epifano, E. et al. High temperature heat capacity of $(U, Am)O_{2\pm x}$. *J. Nucl. Mater.* **494**, 95–102 (2017).

17. Cooper, R. I. & Willis, B. T. M. Refinement of the structure of β-U_4O_9. *Acta Crystallogr A* **60**, 322–325 (2004).

18. Loopstra, B. O. On the crystal structure of α-U_3O_8. *J. Inorg. Nucl. Chem.* **39**, 1713–1714 (1977).

19. Chikalla, T. D. & Eyring, L. Phase relationships in the americium-oxygen system. *J. Inorg. Nucl. Chem.* **30**, 133–145 (1968).

20. Kvashnina, K. O., Butorin, S. M., Martin, P. & Glatzel, P. Chemical state of complex uranium oxides. *Phys. Rev. Lett.* **111**, 253002 (2013).

21. Lebreton, F. et al. New Insight into self-irradiation effects on local and long-range structure of uranium–americium mixed oxides (through XAS and XRD). *Inorg. Chem.* **53**, 9531–9540 (2014).

22. Shannon, R. D. Revised effective ionic radii and systematic studies of interatomic distances in halides and chalcogenides. *Acta Crystallogr. A* **32**, 751–767 (1976).

23. Willis, B. T. M. Positions of the oxygen atoms in $UO_{2.13}$. *Nature* **197**, 755–756 (1963).

24. Willis, B. T. M. The defect structure of hyper-stoichiometric uranium dioxide. *Acta Crystallogr. A* **34**, 88–90 (1978).

25. Allen, G. C., Tempest, P. A. & Tyler, J. W. Coordination model for the defect structure of hyperstoichiometric UO_{2+x} and U_4O_9. *Nature* **295**, 48–49 (1982).

26. Murray, A. D. & Willis, B. T. M. A neutron diffraction study of anion clusters in nonstoichiometric uranium dioxide. *J. Solid State Chem.* **84**, 52–57 (1990).

27. Loopstra, B. O. The structure of β-U_3O_8. *Acta Crystallogr. B* **26**, 656–657 (1970).

28. Loopstra, B. O., Taylor, J. C. & Waugh, A. B. Neutron powder profile studies of the gamma uranium trioxide phases. *J. Solid State Chem.* **20**, 9–19 (1977).

29. Shimanouchi, T., Tsuboi, M. & miyazawa, T. Optically active lattice vibrations as treated by the GF-matrix method. *J. Chem. Phys.* **35**, 1597–1612 (1961).

30. Manara, D. & Renker, B. Raman spectra of stoichiometric and hyperstoichiometric uranium dioxide. *J. Nucl. Mater.* **321**, 233–237 (2003).

31. Livneh, T. & Sterer, E. Effect of pressure on the resonant multiphonon Raman scattering in UO_2. *Phys. Rev. B* **73**, 085118 (2006).

32. Desgranges, L., Baldinozzi, G., Simon, P., Guimbretière, G. & Canizares, A. Raman spectrum of U_4O_9: a new interpretation of damage lines in UO_2. *J. Raman Spectrosc.* **43**, 455–458 (2012).

33. Guimbretière, G. et al. In situ Raman monitoring of He^{2+} irradiation induced damage in a UO_2 ceramic. *Appl. Phys. Lett.* **103**, 041904 (2013).

34. Talip, Z. et al. Raman microspectroscopic studies of unirradiated homogeneous $(U_{0.76}Pu_{0.24})O_{2+x}$: the effects of Pu content, non-stoichiometry, self-radiation damage and secondary phases. *J. Raman Spectrosc.* **48**, 765–772 (2017).

35. Begun, G. M., Haire, R. G., Wilmarth, W. R. & Peterson, J. R. Raman spectra of some actinide dioxides and of EuF_2. *J. Common Met.* **162**, 129–133 (1990).

36. Sarsfield, M. J., Taylor, R. J., Puxley, C. & Steele, H. M. Raman spectroscopy of plutonium dioxide and related materials. *J. Nucl. Mater.* **427**, 333–342 (2012).

37. Schoenes, J. Optical properties and electronic structure of UO_2. *J. Appl. Phys.* **49**, 1463–1465 (1978).

38. Schoenes, J. Electronic transitions, crystal field effects and phonons in UO_2. *Phys. Rep.* **63**, 301–336 (1980).

39. Meek, T. T., von Roedern, B., Clem, P. G. & Hanrahan, R. J. Some optical properties of intrinsic and doped UO_2 thin films. *Mater. Lett.* **59**, 1085–1088 (2005).

40. Yu, S.-W. et al. f-f origin of the insulating state in uranium dioxide: X-ray absorption experiments and first-principles calculations. *Phys. Rev. B* **83**, 165102 (2011).

41. Suzuki, C. et al. Core-hole effect on XANES and electronic structure of minor actinide dioxides with fluorite structure. *J. Phys. Chem. Solids* **73**, 209–216 (2012).

42. Epifano, E. *Study of the U-Am-O ternary phase diagram*. PhD dissertation, Université Paris-Saclay (2017).

43. Lebreton, F., Horlait, D., Delahaye, T. & Blanchart, P. Fabrication and characterization of $U_{1-x}Am_xO_{2\pm\delta}$ compounds with high americium contents (x=0.3, 0.4 and 0.5). *J. Nucl. Mater.* **439**, 99–102 (2013).

44. Rostaing, C., Poinssot, C., Warin, D., Baron, P. & Lorraina, B. Development and validation of the EXAm separation process for single Am recycling. *Procedia Chem.* **7**, 367–373 (2012).

45. Epifano, E. et al. Insight into the Am–O phase equilibria: a thermodynamic study coupling high-temperature XRD and CALPHAD modeling. *Inorg. Chem.* **56**, 7416–7432 (2017).

46. Delahaye, T., Lebreton, F., Horlait, D., Herlet, N. & Dehaudt, P. Application of the UMACS process to highly dense $U_{1-x}Am_xO_{2\pm\delta}$ MABB fuel fabrication for the DIAMINO irradiation. *J. Nucl. Mater.* **432**, 305–312 (2013).

47. Rodríguez-Carvajal, J. Recent developments of the program FULLPROF, commission on powder diffraction. *IUCr Newsl.* **26**, 12–19 (2001).

48. Zimina, A. et al. CAT-ACT—A new highly versatile x-ray spectroscopy beamline for catalysis and radionuclide science at the KIT synchrotron light facility ANKA. *Rev. Sci. Instrum.* **88**, 113113 (2017).

49. Ravel, B. & Newville, M. ATHENA, ARTEMIS, HEPHAESTUS: data analysis for X-ray absorption spectroscopy using IFEFFIT. *J. Synchrotron Radiat.* **12**, 537–541 (2005).

50. Parker, J. H., Feldman, D. W. & Ashkin, M. Raman Scattering by silicon and germanium. *Phys. Rev.* **155**, 712–714 (1967).

Acknowledgements

Author contributions
E.E. designed the study, performed the experiments, analysed the data and wrote the paper. M.N. acquired and analysed the Raman data and he wrote the paper. D.M. acquired and analysed the Raman data and he wrote the paper. A.C.S., C.H. and J.L. performed the XAS experiments. R. J. Konings and C. Guéneau contributed to the discussion and interpretation of the results. P. M. Martin designed the experiment, analysed the data and he wrote the paper. D. Prieur, K. Dardenne, T. Vitova and J. Rothe participated at the measurements at the CAT-ACT beamline.

Additional information
Supplementary information accompanies this paper at https://doi.org/10.1038/s42004-019-0161-0.

Competing interests: The authors declare no competing interests.

Reprints and permission information is available online at http://npg.nature.com/reprintsandpermissions/

Publisher's note: Springer Nature remains neutral with regard to jurisdictional claims in published maps and institutional affiliations.